17 Physics of Biological Systems

Conrad Escher, Hans-Werner Fink, Tatiana Latychevskaia, Jean-Nicolas Longchamp, Marianna Lorenzo, Mirna Saliba (until November 2013), Jonas Verges, Flavio Wicki

in collaboration with: Eugen Ermantraut, Clondiag Chip Technologies GmbH (Germany); Prof. Jannik C. Meyer, University of Vienna (Austria); Prof. Ute Kaiser, University of Ulm (Germany); Prof. Klaus Kern, Max Planck Institut, Stuttgart (Germany); Dr. Ilona Müllerová and Dr. Luděk Frank, Institute of Scientific Instruments, Brno (Czech Republic); Dr. Fabio Lamattina, EMPA Dübendorf (Switzerland)

The structural investigation of individual biological objects by employing coherent low-energy electrons is the primary goal of our research. It involves inline holography with low-energy electrons as well as coherent diffraction imaging and is assisted by micro-structuring techniques using a focused gallium ion beam device as well as a focused helium ion beam available to us at the at the Swiss Federal Laboratories for materials science and technology (EMPA) in Dübendorf. Our current activities are divided in the following interconnected individual projects listed below.

- Electron Holography and Coherent Diffraction
  Major experimental challenges are to improve the interference resolution, establish methods for creating free-standing thin films of graphene transparent for low-energy electrons as well as appropriate techniques to present a single protein to the coherent electron wave. Next to these experimental issues, a second, equally important aspect for achieving high-resolution structural information is the reconstruction of the electron holograms respectively iterative phase retrieval in coherent diffraction. This is achieved by employing newly developed numerical algorithms to solve the integrals governing these coherent optics problems.

- Coherent Diffraction Imaging of Graphene-Supported Single Biomolecules at Atomic Resolution (Ambizione project of Jean-Nicolas Longchamp)
  Methods to deposit biomolecules onto freestanding graphene, in particular in-situ electrospray deposition are to be explored. The successful deposition and imaging of test biomolecules shall be cross-validated by TEM investigations carried out at the microscopy centre of the University of Zurich. Moreover, the possibility to use other two-dimensional materials, as for instance boron nitride, as substrate for low-energy electron microscopy shall also be investigated. Additionally, with the availability of ultra-clean graphene, low-energy electron holographic imaging of the electron transport in freestanding graphene and in particular scattering processes of conduction electrons at grain boundaries or atomic defect shall be explored.

- Electron and Ion Point Sources
  Field Ion Microscopy and related techniques are employed for fabricating and applying bright electron and ion point sources.

- DNA and Proteins in the Liquid Phase
  The aim of this project is to directly observe the dynamics of single DNA molecules in liquids by video fluorescent microscopy. In combination with molecular anchoring techniques, adopted from Clondiag Chip Technologies in Jena, we also address the energetics of a single DNA molecule. Appropriate DNA modifications for attaching fluorescent proteins are also designed by and shall serve us in our efforts to obtain structural information about proteins by electron holography and coherent diffraction. Thermal desorption spectroscopy of water from fluorescent proteins shall help us to judge under what thermal conditions proteins are still in their native state despite the vacuum environment.

Selected recent achievements referring to the past year shall be discussed in some more detail below.

17.1 Overall Motivation and Research Goals

Most of the protein structural information available today has been obtained from crystallography experiments by means of averaging over many molecules assembled into a crystal. Since biological molecules exhibit different conformations, averaging smears out structural details. That is why a strong desire to gain structural data from just a single molecule is emerging. We are working towards the objective of deriving atomic structure information from experiments carried out on just one individual molecule subject to the interaction with a coherent low-energy electron wave. Meanwhile, it has been thoroughly established that electrons with kinetic energies below 200 eV are the only radiation known today where elastic scattering dominates. Radiation damage-free imaging of a single biological molecule is thus pos-

sible by recording holograms and coherent low-energy electron diffraction patterns [1, 2]. So far, we were able to achieve a resolution of 2 Angstroms in imaging a free-standing graphene which appears sufficient to eventually obtain detailed structural information about a single protein.

17.2 Resolution enhancement in digital holography by extrapolation of holograms

It is generally believed that the resolution in digital holography is limited by the size of the captured holographic record. We have developed a method to circumvent this limit by extrapolating experimental holograms beyond the area that is actually captured. This is done by first padding the surroundings of the hologram and then conducting an iterative reconstruction procedure. The wave front beyond the experimentally detected area is thus retrieved and the hologram reconstruction shows enhanced resolution. To demonstrate the power of this concept, we apply it to simulated as well as experimental holograms.

Intrinsic to the principle of holography is that even a fraction of a hologram permits the reconstruction of the entire object [3]. However, in digital holography the overall achievable resolution in the reconstruction is believed to be limited by the size of the captured digital record [4, 5]:

$$R = \frac{\lambda z}{N\Delta_S} \tag{17.1}$$

where λ is the wavelength, z is the distance between object and screen, N is the number of pixels, and Δ_S is the pixel size of the detector. $N\Delta_S \times N\Delta_S$ is thus the size of the hologram and hence the limiting aperture of the optical system. Therefore, in the case of digitally recorded holograms, the detector size appears to limit the achievable resolution. We make use of the basic notion that the interference distribution recorded in a hologram is created by waves that are continuous and must persist beyond the experimentally recorded area. Consequently, it must be possible to extrapolate a truncated hologram beyond the intensity distribution actually recorded in an experiment. Extrapolation of holograms can be achieved by applying an iterative routine using a constraint based on the physical notion that the amplitude of the elastic scattered object wave must not be larger than the amplitude of the incoming wave [6]. After several iterations, the outer part of the hologram, which was initially not available from the experimental record, is retrieved. The availability of these emerging higher-order fringes in such extrapolated holograms leads to an improved resolution in the object reconstruction.

17.2.1 Simulated example

To demonstrate our method we first use the simulated hologram of two point scatterers, as illustrated in Fig. 17.1. The object area is 2×2 mm^2, sampled with 2000×2000 pixels, and the scatterers are separated by six pixels. The hologram is simulated for 500 nm laser light in the inline holographic setup [6, 7], where the distance between the point source and the sample amounts to 4 mm and the distance between the point source and the hologram is 1 m; a screen size of 0.5×0.5 m^2 is used in the simulation. The resultant simulated hologram is shown in Fig. 17.1(b). According to Eq. 17.1, the resolution intrinsic to this simulated hologram amounts to 1 μm

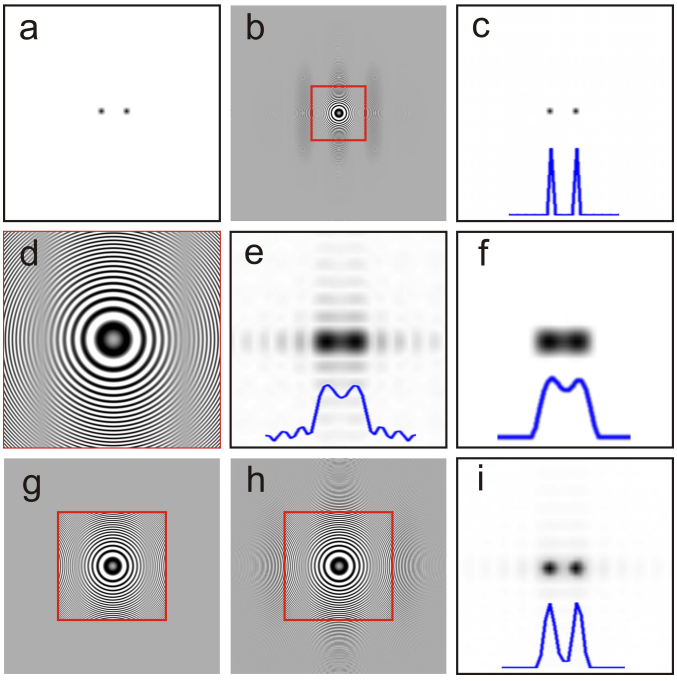

FIG. 17.1 – Simulated example.
(a) Synthetic object, consisting of two point scatterers, separated by six pixels; the central 50×50 pixels region is shown.
(b) Simulated hologram, 2000×2000 pixels in size.
(c) Hologram reconstruction, showing the central 50×50 pixels region.
(d) Selected 500×500 pixels central region of the original hologram, as marked in (b) by a red square.
(e) Reconstruction of (d). (f) Result of iterative reconstruction of (d) after 300 iterations.
(g) The selected 500×500 pixels region is padded to 1000×1000 pixels with a constant background.
(h) Extrapolated hologram after 300 iterations.
(i) Reconstruction of the extrapolated hologram; the central 50×50 pixels region is shown.
The blue curves in (c), (e), (f), and (i) show the intensity profiles of the reconstructions.

and leads to a perfectly resolved reconstruction of the two points separated by 6 μm, as shown in Fig. 17.1(c). To mimic a hologram limited by detector size, the central 500×500 pixels region of the simulated hologram is cut out as displayed in Fig. 17.1(d). The resolution intrinsic to this truncated hologram amounts to 4 μm, as derived from Eq. 17.1. Accordingly, the reconstruction of this truncated hologram results in two smeared-out regions rather than separated points that are barely resolved, as evident from Fig. 17.1(e). Next, the truncated hologram is iteratively reconstructed [6–8] in the following manner. First, the surroundings of the hologram are filled with a constant background, leading to a padded record of 1000×1000 pixels, as shown in Fig. 17.1(g). For the first iteration, the phase distribution in the hologram plane is given by the phase distribution of the reference wave. During the iterative reconstruction the following constraints are applied. First, in the hologram plane, the amplitude of the central 500×500 pixels region is replaced by the already known data and the values of the outer pixels are updated after each iteration. Second, in the object plane, the object is confined within a limited region by applying an oval mask; the signal outside the mask is set to zero and then a positive absorption filter is applied [6]. After 300 iterations, not only does the holographic image extrapolate itself beyond the 500×500 region, as evident from Fig. 17.1(h), but also the reconstruction of such a extrapolated hologram reveals that the two points are now clearly resolved, as can be seen in Fig. 17.1(i). A theoretical resolution of 2 μm estimated by Eq. 17.1 is observed in the reconstruction. To verify that the effect of the resolution enhancement is not due to the iterative retrieval itself, we also applied the same iterative reconstruction to the non-padded 500×500 pixels truncated hologram. Its reconstruction after 300 iterations, shown in Fig. 17.1(f), does not differ much from the reconstruction shown in Fig. 17.1(e). While the twin image is suppressed, the two points remain barely resolved. The reason is that when there is a larger area available in the hologram plane, the series of wavelets constituting the wavefront in the hologram plane can be fitted better. This hypothesis is confirmed by a closer look at the intensity distributions in the hologram plane. During the iterative procedure the intensity distribution in the hologram is replaced by an "experimental" distribution after each iteration and thus iteratively approaches the "experimental" distribution. The mismatch between the "experimental" amplitude distribution and the amplitude distribution updated after each iteration is quantitatively described by the error function. Fig. 17.2 shows the intensity profiles in the hologram plane: even after 300 iterations the 500×500 pixels truncated hologram does not match the intensity distribution of the original hologram. But the intensity profile of the extrapolated 1000×1000 pixels hologram obtained after

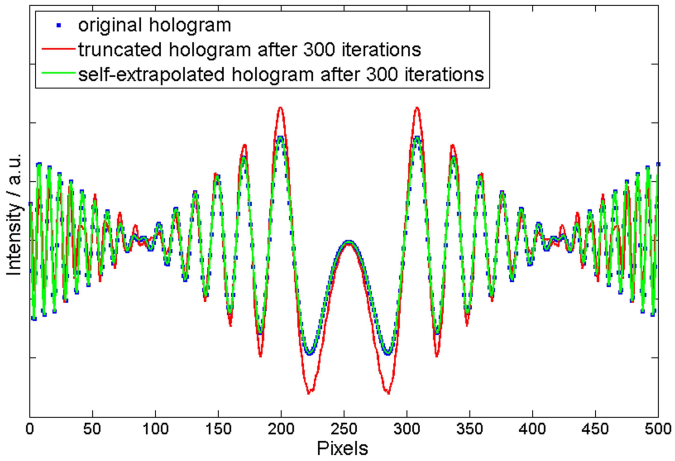

FIG. 17.2 – Profiles of the intensity in the central region of the holograms: original hologram (blue dots), 500×500 pixels truncated hologram after 300 iterations (red line), and 1000×1000 extrapolated hologram after 300 iterations.

300 iterations matches the original distribution perfectly. Thus, when a larger area in the hologram plane where the intensities can be varied is available, a better agreement between the "experimental" and the fitted hologram can be achieved. Although the numerical experiments clearly show that the resolution can be enhanced by extrapolation of the hologram, the enhancement cannot be extended to infinity. We also tried padding from 500×500 pixels to the original value of 2000×2000 pixels, but this only marginally improves the resolution when compared to the resolution obtained by padding only up to 1000×1000 pixels.

17.2.2 Experimental example

We also performed experimental tests of our method using an optical hologram recorded in an inline scheme shown in Fig. 17.3. The optical hologram was recorded using 523 nm laser light; the sample was placed 0.25 mm in front of the divergent source, the distance between source and screen was 75 mm, the size of the hologram was 35×35 mm^2, and it was sampled with 1000×1000 pixels. The sample consisting of four circles with diame-

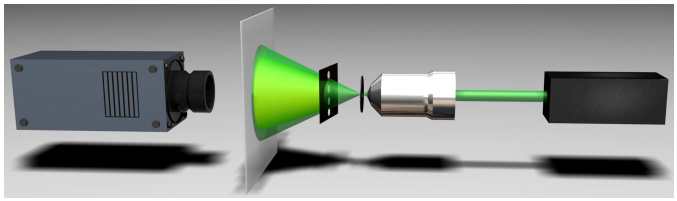

FIG. 17.3 – Experimental scheme for recording optical inline holograms

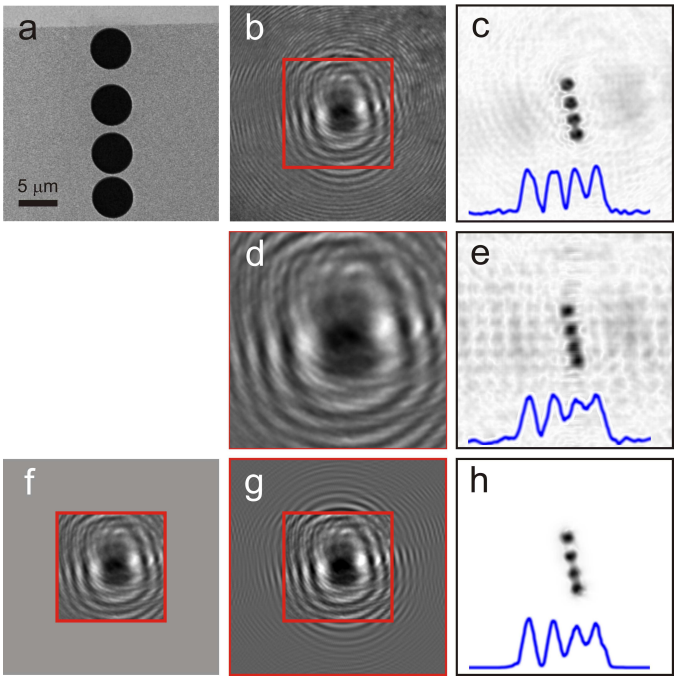

FIG. 17.4 – Experimental verification of the method.
(a) Scanning electron microscope image of the sample.
(b) 1000×1000 pixels experimental optical hologram of the sample and
(c) its reconstruction; the 500×500 pixels central part is shown.
(d) Selected 500×500 pixels central region of the experimental hologram, and
(e) its reconstruction.
(f) The 500×500 pixels hologram padded to 1000×1000 pixels.
(g) The 1000×1000 pixels extrapolated hologram after 100 iterations.
(h) Reconstruction of the extrapolated hologram.
The 500×500 pixels central part is shown. The blue curves in (c), (e) and (h) show the intensity profiles of the reconstructions.

ters of 5 μm each was created by focused ion beam milling in a silicon nitride membrane covered with a 200 nm platinum layer and is shown in Fig. 17.4(a). The experimental hologram is shown in Fig. 17.4(b) and its reconstruction is displayed in Fig. 17.4(c).

When the central region of the hologram corresponding to 500×500 pixels is cut out (Fig. 17.4(d)), the reconstruction of this truncated hologram results in a blurred image of the four circles, shown Fig. 17.4(e). Next, the truncated hologram is padded up to 1000×1000 pixels, as shown in Fig. 17.2(f), and iteratively reconstructed as described above. After every five iterations the reconstructed amplitude was convolved with a 3×3 pixels kernel in the form of a Gaussian distribution to smooth and suppress the accumulation of noisy peaks. After 100 iterations, higher order fringes emerge (see Fig. 17.4(g)), and the reconstruction of the extrapolated hologram exhibits better resolved circles, shown in Fig. 17.4(h).

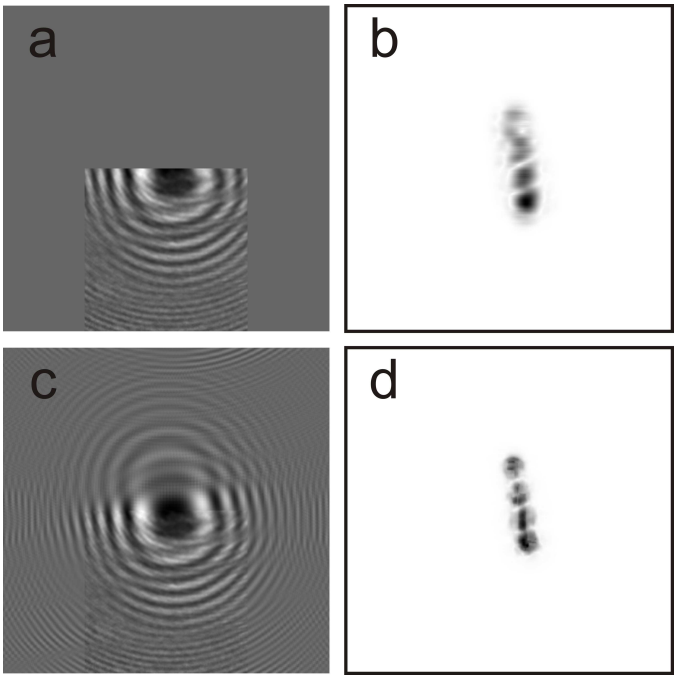

FIG. 17.5 – Extrapolation of a piece of the hologram.
(a) The selected 500×500 pixels part of the hologram is padded up to 1000×1000 pixels; and
(b) its reconstruction; the 500×500 pixels central part is shown.
(c) 1000×1000 pixels extrapolated hologram after 300 iterations and
(d) its reconstruction; the 500×500 pixels central part is shown.

It is also possible to extrapolate a hologram when a significant low-resolution part is missing. To demonstrate it, we cropped the 500×500 pixels lower part of the experimental hologram and padded it up to 1000×1000 pixels (see Fig. 17.5(a)). The corresponding reconstruction presented in Fig. 17.5(b) does not show all four circles. Next, we applied the iterative extrapolation routine; after 300 iterations the hologram had extrapolated itself (see Fig. 17.5(c)), and the reconstruction clearly shows four circles (see Fig. 17.5(d)). Aside from the intensity variations within the reconstructed circles the agreement with the original object is good. The variations in artifact intensity indicate the limits of the method; thus it is better to use the experimentally recorded holographic information when available.

In conclusion, the method presented above improves the resolution of holographic reconstructions by extrapolation of the digital hologram beyond the actual detector size. The method can be applied provided the following conditions are fulfilled:

- The interference pattern is only limited by the size of the detector; in other words, there is an interference pattern at the edges of the hologram.
- The object under study occupies a limited area and thus can be masked in the iterative reconstruction.
- The object has a finite thickness in the z-dimension, which allows an iterative retrieval by field propagation between two planes: the hologram and object planes.
- The available part of the hologram exhibits high dynamics in the intensity distribution. The latter requirement can be explained in terms of the resolution provided by the smallest scatterers whose scattered wave signal is present over the entire hologram area and needs to be detected in the available piece of the hologram. This high-resolution information eventually allows hologram extrapolation and retrieval of the entire object at enhanced resolution.

17.3 Low-energy electron holographic imaging of gold nanorods supported by ultraclean graphene

An ideal support for electron microscopy shall be as thin as possible and interact as little as possible with the primary electrons. Since graphene is atomically thin and made up of carbon atoms arranged in a honeycomb lattice, the potential to use graphene as substrate in electron microscopy is enormous. Until now graphene has hardly ever been used for this purpose because the cleanliness of freestanding graphene before or after deposition of the objects of interest was insufficient. We demonstrate here by means of low-energy electron holographic imaging that freestanding graphene prepared with the platinum-metal catalysis method remains ultraclean even after re-exposure to ambient conditions and deposition of gold nanorods from the liquid phase. In the holographic reconstruction of the gold particles the organic shell surrounding the objects is apparent while it is not detectable in SEM images of the very same sample, demonstrating the tremendous potential of low-energy electron holography for the imaging of graphene-supported single biomolecules.

To be imaged by means of electron microscopy, an object is normally placed onto a substrate. The signal from the object support, arising from the scattering of the impinging primary electrons in transmission electron microscopy, or from the creation of secondary electrons in a scanning electron microscope, is spurious and efforts to reduce these signals have been accomplished since the development and implementation of the first electron microscopes. Ideally, for maximal contrast and resolution, one would like to have the thinnest substrate possible, made up of a low-atomic-number material, in order to reduce the interaction volume and the scattering cross-section of the incoming electrons [9, 10]. The idea of using freestanding single-layer graphene as such ultimate microscopic sample carrier in electron microscopy [11–17] has been around since the isolation of single-layer graphene was achieved in 2004 by Geim and Novoselov [18, 19]. Significant efforts have been undertaken in the past few years to develop techniques for preparing either exfoliated or CVD grown graphene in a freestanding form [17, 20–23]. Unfortunately, the cleanliness of the prepared graphene sheets has never been satisfactory with regards to their use as sample carrier [17, 22, 24, 25]. Only recently, it has become possible to prepare ultraclean freestanding graphene by platinum-metal catalysis [26]. Compared to previous methods, the one applied here leads to large regions, extending up to several square microns of atomically clean freestanding graphene suitable for use in electron microscopy [2, 26, 27]. We were able to show that freestanding graphene prepared by the platinum-metal catalysis method remains clean, even after re-exposure to ambient pressure and subsequent wet deposition of nanometre-sized gold rods. We present low-energy electron holograms of gold nanorods on graphene and cross-validate the presence of the nanorods by scanning electron imaging of the very same sample. Moreover, we compare the appearance of the rods when either imaged with low-energy electron holography or by means of a scanning electron microscope (SEM).

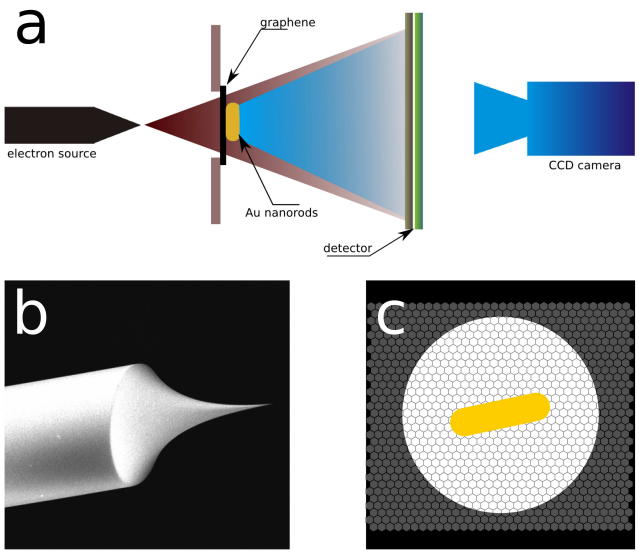

FIG. 17.6 –
(a) The setup for low-energy electron holography. The source-sample distance is 100 – 1000 nm which leads to electron energies of 50 – 250 eV. The distance between sample and detector is 68 mm. The detector diameter is 75 mm, which represents an acceptance angle of 29°.
(b) SEM image of an electrochemically etched W(111) tip acting as field-emitter of a divergent coherent low-energy electron beam.
(c) A gold nanorod lying on ultraclean freestanding graphene suspended over a round hole.

17.3.1 Materials and Methods

Ultraclean freestanding graphene, covering holes of 500 nm in diameter milled in a silicon nitride membrane, is prepared by the platinum-metal catalysis method [26]. The cleanliness of the as-prepared graphene is then inspected in a low-energy electron point source microscope operated under UHV conditions (Fig. 17.6). In this holographic setup, inspired by Gabor's original idea of in-line holography [3, 8, 28], a sharp (111)-oriented tungsten tip acts as source of a divergent beam of highly coherent electrons [29–32]. The electron emitter can be brought as close as 200 nm to the sample with the help of a 3-axis nanopositioner. Part of the electron wave impinging onto the sample is elastically scattered and represents the object wave, while the un-scattered part of the wave represents the reference wave [33]. At a distant detector, the interference pattern of the two waves – the hologram – is recorded. The magnification in the image is given by the ratio of detector-tip-distance to sample-tip-distance and is of the order of 10^6.

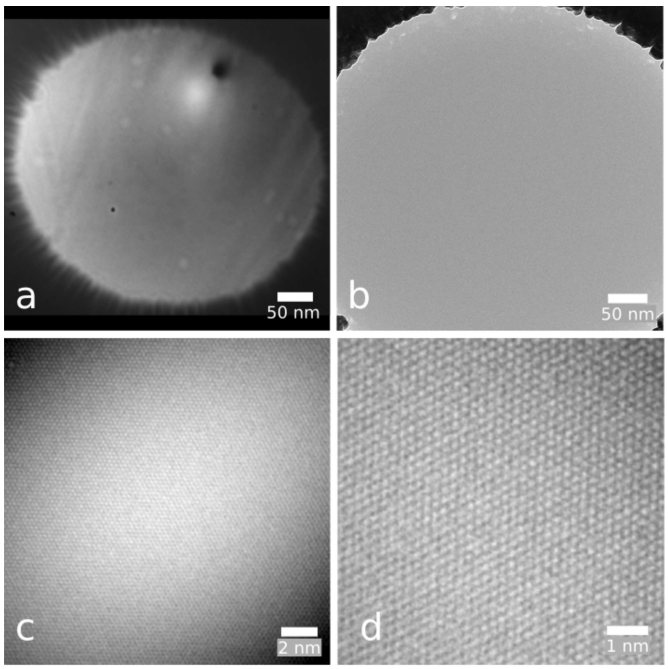

17.3.2 Results and Discussion

Fig. 17.7(a) shows an example of a hole of 500 nm in diameter covered by a single layer of ultraclean graphene, imaged by low-energy electrons. Only the observation of interference fringes, arising due to the presence of a few hydrocarbons less than 1 nm in size, reveals the existence of graphene covering the hole [26]. The cleanliness of the as-prepared graphene has also been investigated by means of high-resolution transmission electron microscopy (TEM) at 80 kV in order to give the reader the possibility to compare the quality of the cleanliness with former TEM results. Fig. 17.7(b) shows a TEM image of graphene, uniformly covering the entire freestanding region, and it is only by imaging the hexagonal atomic arrangement (Fig. 17.7(c)) that the presence of graphene can reliably be confirmed.

FIG. 17.7 –
(a) Low-energy (62 eV) electron transmission image of ultraclean freestanding graphene covering a hole of 500 nm in diameter milled in a silicon nitride membrane.
(b) 80 kV TEM imaging of ultraclean graphene covering a hole of 500 nm in diameter milled in a silicon nitride membrane.
(c) High-resolution TEM imaging of a 19x19 nm^2 region of ultraclean freestanding graphene, the unit cell arrangement is visible and the atomic cleanliness of the graphene is conserved over the whole freestanding area.
(d) High-resolution TEM imaging of a 8x8 nm^2 region of ultraclean freestanding graphene.
TEM data by courtesy of Gerardo Algara-Siller from the University of Ulm.

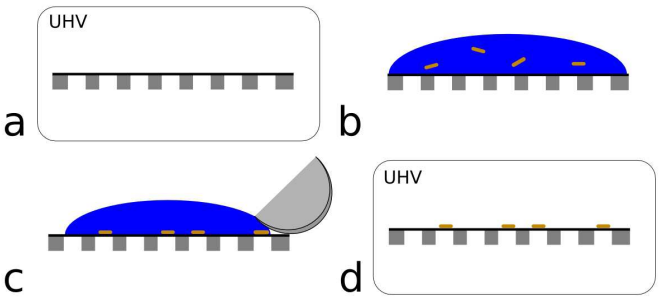

FIG. 17.8 –
(a) The cleanliness of the graphene sample carrier is first inspected by means of low-energy electron holography under UHV conditions.
(b) A drop of the solution containing gold nanorods is applied onto the substrate.
(c) After waiting a few seconds for the sedimentation of the gold nanorods onto the graphene, the excess water is removed with a filter paper.
(d) Before the re-insertion in the UHV low-energy electron microscope, the sample is re-heated to 200^{o}C for 30 min. The nanorods are now ready to be imaged by means of low-energy electron holography.

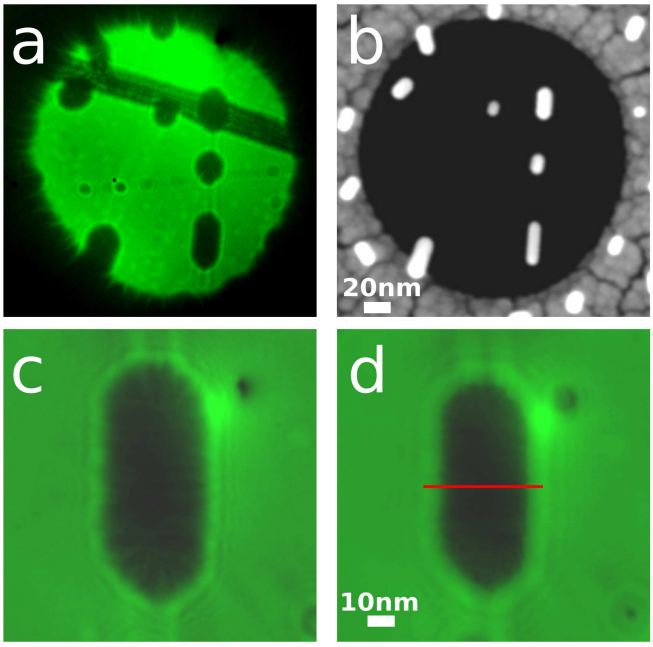

FIG. 17.9 –
(a) Low-energy electron hologram (93 eV) of gold nanorods lying on freestanding graphene. The graphene remained clean even after the deposition of the nanorods.
(b) SEM image (7 kV) of the very same sample presented in (a).
(c) High-magnification low-energy electron hologram (58 eV) of the nanorod on the lower right side presented in (a) and (b).
(d) The shape of the gold nanorod is reconstructed from the hologram in (c) at a source-sample distance of 182 nm. An intensity profile along the red line is displayed in Fig. 17.10.

For the deposition of gold nanorods, a graphene sample prepared as described above is taken out of the low-energy electron microscope. Under ambient conditions, a drop of a 0.5 nm gold nanorod aqueous solution [34] is subsequently applied onto the graphene (Fig. 17.8(b)). A few seconds were given for the rods to sediment before the excess water was removed with filter paper (Fig. 17.8(c)). Prior to the re-introduction of the sample into the electron microscope, the sample is kept at 200^{o}C for 30min.

Fig. 17.9(a) shows an electron hologram of gold nanorods on freestanding graphene recorded with 93 eV kinetic energy electrons. The graphene surrounding the rods remained clean even after the re-exposition to ambient pressure and the deposition of the gold particles from the liquid phase. In Fig. 17.9(b) a SEM image (7 kV) of the very same sample is presented. The nanorods can be associated one-to-one with the objects observed in the holographic image presented in Fig. 17.9(a). The yield of secondary electrons produced by the graphene substrate is so low that the rods, shown in Fig. 17.9(b), seem to levitate, demonstrating the utility of graphene as a substrate for scanning electron microscopy. A high-magnification hologram (58 eV) of a gold nanorod is presented in Fig. 17.9(c) along with its reconstruction, see Fig. 17.9(d), obtained as described in [5, 7]. The object presented in these two images is the very same gold nanorod observed in Fig. 17.9(a) in the low right corner. The remaining interference fringes that can be observed around the object in the reconstruction (Fig. 17.9(d)) are due to the presence of the out-of-focus twin image [6]. The size of the rod in Fig. 17.9(d) accounts for a width of 30 nm and a length of 72 nm. While the length in the holographic reconstruction image matches perfectly the length that can be measured in the SEM image, a discrepancy opens up when one compares the width measured in the two images (30 nm in the holographic reconstruction and 21 nm in the SEM image). We associate this discrepancy with the fact that the gold rods feature an organic coat in order to be soluble in aqueous solution [34]. This organic layer, however, is only present along the rods but not at the face sides. The several-nanometre thick methyl-shell cannot be imaged in an SEM because of the low contrast that it produces and because of the radiation damage provoked by the high-energy electrons. In low-energy electron holography the electron scattering cross-section depends only very weakly on the atomic number, therefore, the organic shell yields a substantial signal. Similarly, in Fig. 17.9(a) a graphene nanoribbon, most likely produced during the CVD growth process, can be detected by low-energy electron holography while it cannot be seen in the SEM image. In Fig. 17.9(d), a plateau at the upper part of the rod and a tip-like shape at the lower part are visible. These observations are in accordance with TEM obser-

vations on similar gold nanorods [35]. The terminations of the rods can adopt different configurations in order to reduce the surface free energy. The plateau shape corresponds to a termination with a 001 facet. The tip shape termination is probably due to a very small 001 terrace surrounded by extended 111 facets forming the conical shape of this termination [35, 36]. The geometrical details of the termination of the gold nanorods are accessible in low-energy electron holography imaging; the resolution of an SEM is insufficient to reveal them.

In Fig. 17.10, an intensity profile along the red line in Fig. 17.9(d) is displayed. The intensity oscillations that can be observed around the region corresponding to the nanorod are due to presence of the out-of focus twin image. In order to assign an upper limit for the resolution obtained in the reconstruction of the gold nanorod (Fig. 17.9(d), one may assume a sharp edge between the nanorod and the substrate. An estimate for the resolution is then given by the distance between 10 and 90% of the maximum intensity [37] measured at the edge and amounts to 1.8 nm. This estimation is rather conservative because of the presence of the organic shell around the gold nanorod. Certainly, this shell does not represent an ideal sharp edge but the slight transmission through the organic shell tends to underestimate the resolution power. A resolution of $1-1.5$ nanometres is probably a more realistic estimation for the resolution that can be obtained in our low-energy electron holography set-up.

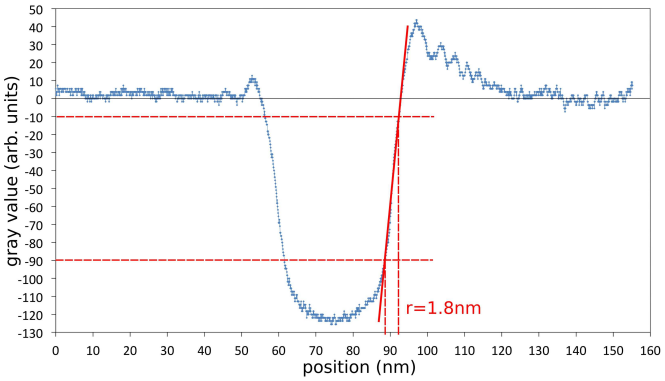

FIG. 17.10 – Intensity profile across the whole reconstructed area of a gold nanorod lying on graphene (Fig. 17.9(d), red line). The resolution in the image is estimated by applying a linear fit to the edge response and amounts to 1.8 nm.

[1] M. Germann *et al.*, Phys. Rev. Lett., (2010) 104(9) 095501.

[2] J.-N. Longchamp *et al.*, Phys. Rev. Lett., (2013) 110(25) 255501.

[3] D. Gabor, Nature, (1948) 161(4098) 777.

[4] U. Schnars and W. Jueptner, *Digital holography*, (2005) Springer.

[5] T. Latychevskaia, J.-N. Longchamp, and H.-W. Fink, Opt. Express, (2012) 20(27) 28871.

[6] T. Latychevskaia and H.-W. Fink, Phys. Rev. Lett., (2007) 98(23) 233901.

[7] T. Latychevskaia and H.-W. Fink, Opt. Express, (2009) 17(13) 10697.

[8] T. Latychevskaia *et al.*, Ultramicroscopy, (2010) 110(5) 472.

[9] L. Reimer, *Transmission electron microscopy*, (1989).

[10] W.H. Dobelle and M. Beer, J. Cell Biol., (1968) 39(3) 733.

[11] R.R. Nair *et al.*, Appl. Phys. Lett., (2010) 97(15) 153102.

[12] K.W. Urban, Nature Mater., (2011) 10(3) 165.

[13] J.Y. Mutus *et al.*, New J. Phys., (2011) 13 063011.

[14] J.C. Meyer *et al.*, Nature, (2007) 446(7131) 60.

[15] N.R. Wilson *et al.*, ACS Nano, (2009) 3(9) 2547.

[16] J.H. Warner *et al.*, ACS Nano, (2010) 4(1) 470.

[17] J.C. Meyer *et al.*, Nature, (2008) 454(7202) 319.

[18] K.S. Novoselov *et al.*, Science, (2004) 306(5696) 666.

[19] K.S. Novoselov *et al.*, Proc. Natl. Acad. Sci. USA, (2005) 102(30) 10451.

[20] Y. Lee *et al.*, Nano Lett., (2010) 10(2) 490.

[21] J.C. Meyer, J.C., *et al.*, Solid State Commun., (2007) 143(1-2) 101.

[22] Z.H. Ni *et al.*, J. Raman Spectrosc., (2010) 41(5) 479.

[23] R.S. Pantelic *et al.*, J. Struct. Biol., (2010) 170(1) 152.

[24] R.S. Pantelic *et al.*, Solid State Commun., (2012) 152(15) 1375.

[25] Y.C. Lin *et al.*, ACS Nano, (2011) 5(3) 2362.

[26] J.-N. Longchamp, C. Escher, and H.-W. Fink, J. Vac. Sci. Technol. B, (2013) 31 020605.

[27] J.-N. Longchamp *et al.*, Appl. Phys. Lett., (2012) 101(11) 113117.

[28] D. Gabor, Holography. Nobel Lecture, (1971).

[29] H.-W. Fink, W. Stocker, and H. Schmid, Phys. Rev. Lett., (1990) 65(10) 1204.

[30] H.-W. Fink, Ultramicroscopy, (1993) 50(1) 101.

[31] H.-W. Fink, IBM Journal of Research and Development, (1986) 30(5) 460.

[32] H.-W. Fink, W. Stocker, and H. Schmid, J. Vac. Sci. Technol., (1990) 8(6) 1323.

[33] H.J. Kreuzer *et al.*, (1992) 45(3-4) 381.

[34] J. Perez-Juste *et al.*, Coord. Chem. Rev., (2005) 249(17-18) 1870.

[35] Z.L. Wang *et al.*, Surf. Sci., (1999) 440(1-2) L809.

[36] H. Katz-Boon *et al.*, Ultramicroscopy, (2013) 124 61.

[37] S.W. Smith, The Scientist & Engineer's Guide to Digital Signal Processing, (1997) San Diego California, California Techical Pub.